Electrospun Nanofibers of *p*-Type NiO/*n*-Type ZnO Heterojunctions with Enhanced Photocatalytic Activity

Zhenyi Zhang, Changlu Shao,* Xinghua Li, Changhua Wang, Mingyi Zhang, and Yichun Liu

Center for Advanced Optoelectronic Functional Materials Research and Key Laboratory of UV Light-Emitting Materials and Technology of Ministry of Education, Northeast Normal University, 5268 Renmin Street, Changchun 130024, People's Republic of China

ABSTRACT One-dimensional electrospun nanofibers of *p*-type NiO/*n*-type ZnO heterojunctions with different molar ratios of Ni to Zn were successfully synthesized using a facile electrospinning technique. X-ray diffraction (XRD), scanning electron microscopy (SEM), energy-dispersive X-ray (EDX) spectroscopy, transmission electron microscopy (TEM), X-ray photoelectron spectroscopy (XPS), UV−vis diffuse reflectance (DR) spectroscopy, resonant Raman spectroscopy, photoluminescence (PL) spectroscopy, and surface photovoltage spectroscopy (SPS) were used to characterize the as-synthesized nanofibers. The results indicated that the *p*−*n* heterojunctions formed between the cubic structure NiO and hexangular structure ZnO in the NiO/ZnO nanofibers. Furthermore, the photocatalytic activity of the as-electrospun NiO/ZnO nanofibers for the degradation of rhodamine B (RB) was much higher than that of electrospun NiO and ZnO nanofibers, which could be ascribed to the formation of *p*−*n* heterojunctions in the NiO/ZnO nanofibers. In particular, the *p*-type NiO/*n*-type ZnO heterojunction nanofibers with the original Ni/Zn molar ratio of 1 exhibited the best catalytic activity, which might be attributed to their high separation efficiency of photogenerated electrons and holes. Notably, the electrospun nanofibers of *p*-type NiO/*n*-type ZnO heterojunctions could be easily recycled without a decrease of the photocatalytic activity due to their one-dimensional nanostructural property.

KEYWORDS: ZnO • NiO • electrospinning • nanofibers • heterojunction • photocatalysis

1. INTRODUCTION

During previous decades, photocatalysis, as a "green" technique, has been extensively used in the area of environmental remediation because various kinds of pollutants can be decomposed completely by photocatalytically active semiconductors under light irradiation (1, 2). With the steady and fast growing field of nanoscience and nanotechnology, the nanostructural semiconductor metal oxides have become the promising photocatalysts in environmental remediation due to their easy availability, nontoxic nature, and biological and chemical stability (3−5). Among those nanostructural semiconductor metal oxides, zinc oxide (ZnO) nanomaterials, naturally *n*-type semiconductors with a wide bandgap (E_g = 3.37 eV), have been recognized as excellent materials for photocatalytic processes due to their high photosensitivity, high catalytic activity, suitable bandgap, low cost, and environmental friendliness (6−9). However, enhancing the photocatalytic efficiency of ZnO nanocatalysts to meet the practical application requirements is still a challenge because of the bottleneck of poor quantum yield caused by the fast recombination rate of photogenerated electron−hole pairs (10). Therefore, many efforts have been developed to increase the separation efficiency of photogenerated electron−hole pairs of ZnO nanocatalysts. Research found that ZnO-based heterojunctions, such as metal (Ag, Au, Pt, etc.)/ZnO and semiconductor (TiO_2, SnO_2, CdS, NiO, etc.)/ZnO heterojunctions, could obviously suppress the recombination of photogenerated electron−hole pairs by the mutual transfer of photogenerated electrons or holes in the heterojunctions (11−15).

Among these composite materials, the NiO/ZnO heterostructural nanomaterials attract much interest in particular because of NiO, as a *p*-type semiconductor (E_g = 3.5 eV), which possesses high *p*-type concentration, high hole mobility, and low lattice mismatch with ZnO, which is beneficial for the formation of *p*−*n* heterojunction with ZnO (16−18). Theoretically, when the *p*-type and *n*-type semiconductor form *p*−*n* heterojunctions, the inner electric field will be formed in the interface of *p*−*n* heterojunctions. At equilibrium, the inner electric field makes the *p*-type semiconductor region have a negative charge, while the *n*-type semiconductor region has a positive charge (19). When the *p*−*n* heterojunction is radiated by ultraviolet (UV) light with the photon energy higher or equal to the band gaps of *p*-type and *n*-type semiconductors, the photogenerated electrons can move to the conduction band (CB) of *n*-type semiconductors and the photogenerated holes to the valence band (VB) of *p*-type semiconductors due to the formation of an inner electric field. Thus, the formation of a *p*-type NiO/*n*-type ZnO heterojunction might hinder the recombination of photogenerated electron−hole pairs and improve the photocatalytic efficiency.

* Corresponding author. Tel.: 8643185098803. E-mail: clshao@nenu.edu.cn.
Received for review July 15, 2010 and accepted September 27, 2010

DOI: 10.1021/am100618h

2010 American Chemical Society

On the other hand, the separation of the nanostructural photocatalysts from the solution after reaction is another challenge in a practical photocatalytic process. Many studies found that the semiconductor metal oxide electrospun nanofiber photocatalysts possessed high photocatalytic activity and favorable recycling characteristics due to their one-dimensional (1D) nanostructural property. These electrospun nanofiber photocatalysts are deemed potentially good candidates for practical applications (20−22). In particular, the electrospun nanofibers of ZnO-based heterojunctions, such as Ag/ZnO, SnO_2−ZnO heterojunctions nanofibers, and so on, have been of immense interest in recent years due to their enhanced photocatalytic activity and favorable recycling characteristics (23−25). However, the photocatalysis performances based on the electrospun nanofibers of *p*-type NiO/*n*-type ZnO heterojunctions have not been explored until now.

In the present work, we report a successful attempt for the fabrication of *p*-type NiO/*n*-type ZnO heterojunction nanofibers using the electrospinning method. It was found that the *p*-type NiO/*n*-type ZnO heterojunction nanofibers exhibited excellent photocatalytic activity superior to the electrospun NiO and ZnO nanofibers, which could be ascribed to the high separation efficiency of photogenerated electron−hole pairs from the *p*−*n* heterojunction. Moreover, due to the large length-to-diameter ratio, the as-electrospun nanofibers could be reclaimed easily by sedimentation without a decrease in photocatalytic activity.

2. EXPERIMENTAL SECTION

2.1. Preparation of the *p*-Type NiO/*n*-Type ZnO Heterojunction Nanofibers. In a typical procedure, the nanofibers of *p*-type NiO/*n*-type ZnO heterojunctions were synthesized using an electrospinning and calcination method. It is described as follows: First, 1.2 g of acetate salt with nickel acetate [$Ni(CH_3COO)_2 \cdot 4H_2O$]/zinc acetate [$Zn(CH_3COO)_2 \cdot 2H_2O$] molar ratios of 0.5 and 1 were mixed with 37 mL of *N*,*N*-dimethylformamide (DMF) in a glovebox under vigorous stirring for 30 min. Subsequently, 6 g of polyacrylonitrile (PAN; M_w = 500 000) was added to the above solution. After stirring at room temperature for 12 h, the precursor solution of the PAN/$Ni(CH_3COO)_2$/$Zn(CH_3COO)_2$ composite was obtained. Subsequently, the above precursor solutions were drawn into a hypodermic syringe. The positive terminal of a variable high-voltage power supply was connected to the needle tip of the syringe while the other terminal was connected to the collector plate. The positive voltage applied to the tip was 10 kV, and the distance between the needle tip and the collector was 10 cm, resulting in a dense web of the electrospun composite nanofibers of PAN/$Ni(CH_3COO)_2$/$Zn(CH_3COO)_2$ being collected on the aluminum foil. Afterward, the above composite nanofibers were calcined at a rate of 25°/h and remained for 2 h at 550 °C. Thus, *p*-type NiO/*n*-type ZnO heterojunction nanofibers with different Ni/Zn molar ratios were successfully prepared. Moreover, to investigate the structure and photocatalytic activity of the *p*-type NiO/*n*-type ZnO heterojunction nanofibers, pure NiO and ZnO nanofibers were prepared using the same experimental conditions. In the following discussion, the *p*-type NiO/*n*-type ZnO heterojunction nanofibers with original Ni/Zn molar ratios of 0.5 and 1 were denoted as NZ1 and NZ2 nanofibers, respectively.

2.2. Characterization. X-ray diffraction (XRD) measurements were carried out using a D/max 2500 XRD spectrometer (Rigaku) with a Cu Kα line of 0.1541 nm. Scanning electron microscopy (SEM; XL-30 ESEM FEG, Micro FEI Philips) and high-resolution transmission electron microscopy (HRTEM; JEOL JEM-2100) were used to characterize the morphologies of the products. X-ray photoelectron spectroscopy (XPS) was performed on a VG-ESCALAB LKII instrument with a Mg Kα ADES ($h\nu$ = 1253.6 eV) source at a residual gas pressure below 10^{-8} Pa. UV−vis diffuse reflectance (DR) spectroscopy of the samples was recorded on a Cary 500 UV−vis−NIR spectrophotometer. The photoluminescence (PL) and resonant Raman spectroscopy of photocatalysts were detected with a Jobin Yvon HR800 micro-Raman spectrometer using a 325 nm line from a He−Cd laser. The surface photovoltage spectroscopy (SPS) instrument was similar to that described in the literature (26). During the process, the sample was put between the indium tin oxide (ITO) and stainless steel electrodes to form a sandwich structured photovoltage cell.

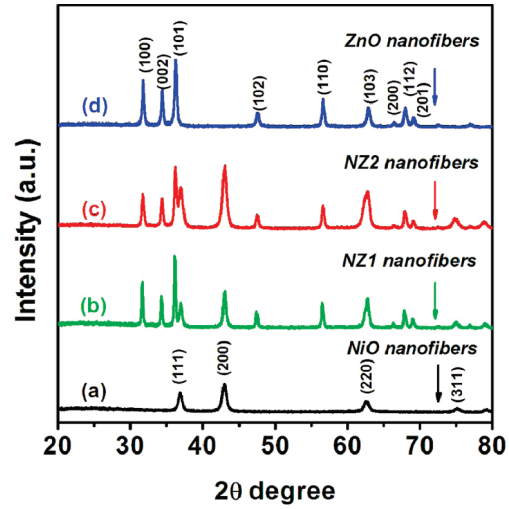

FIGURE 1. XRD patterns of the electrospun nanofibers: (a) NiO nanofibers, (b) NZ1 nanofibers, (c) NZ2 nanofibers, (d) ZnO nanofiber.

2.3. Photocatalytic Test. The photoreactor was designed with an internal light source surrounded by a quartz jacket (50 W high pressure mercury lamp with main emission wavelength 313 nm and an average light intensity of 2.85 mW cm^{-2}), where the suspension included the nanofiber catalyst (0.01g), and an aqueous RB (100 mL, 10 mg/L) completely surrounded the light source. The suspension was stirred in the dark for 30 min to obtain a good dispersion and establish adsorption−desorption equilibrium between the organic molecules and the catalyst surfaces. The acidity of the suspension was neutral. The temperature of the suspension was maintained at 30 ± 2°C by circulating water through an external cooling coil, and the system was open to the air. Decreases in the concentrations of dyes were analyzed using a Cary 500 UV−vis−NIR spectrophotometer at λ = 553 nm. At given intervals of illumination, the samples of the reaction solution were taken out and then centrifuged and filtered. Finally, the filtrates were analyzed.

3. RESULTS AND DISCUSSION

The X-ray diffraction (XRD) patterns of the as-electrospun nanofibers are shown in Figure 1. All diffraction peaks in Figure 1a and d could be perfectly indexed as the cubic structure for NiO (JCPDS-78-0643) and hexagonal structure for ZnO (JCPDS 36-1451), respectively. Furthermore, the diffraction peaks of the NiO and ZnO nanofibers were sharp and intense, indicating the highly crystalline character of the nanofibers. As observed in Figure 1b and c, two sets of diffraction peaks existed for NZ1 and NZ2 nanofibers, which

Table 1. Physicochemical Properties of the As-Electrospun Nanofibers

sample	grain size (nm)	diameter (nm)	amount used for test (g)
NiO nanofibers	13.5	93 ± 15	0.01
NZ1 nanofibers	17.8−31.4	61 ± 11	0.01
NZ2 nanofibers	14.9−29.6	68 ± 15	0.01
ZnO nanofibers	32.4	128 ± 14	0.01
TiO_2 nanofibers	15.7	346 ± 85	0.01

were correspondingly ascribed to the cubic structure NiO and hexagonal structure ZnO. In addition, the diffraction peaks of NiO were strengthened gradually when increasing the original molar ratio of Ni to Zn from 0.5 to 1 in the NiO/ZnO nanofibers (from NZ1 to NZ2 nanofibers). No characteristic peaks for impurity were observed, suggesting that the composition of the above nanofibers was NiO and ZnO. Moreover, the average grain sizes of the products were calculated by applying the Debye−Scherrer formula and are listed in Table 1. It can be seen that the average grain size of NiO and ZnO nanoparticles was about 13.5−17.8 and 29.6−32.4 nm, respectively, in the as-electrospun nanofibers. It is worthwhile to note that the diffraction peaks of NiO and ZnO in the NZ1 and NZ2 nanofibers were still sharp and intense, implying the high crystallinity of the nanofibers after calcining at 550 °C for 2 h.

Figure 2A and B show the typical scanning electron microscopy (SEM) images of the as-electrospun NZ1 and NZ2 nanofibers, respectively. It could be seen that these randomly oriented nanofibers had a rough surface after calcinations at 550 °C due to the decomposition of PAN. The lengths of NZ1 and NZ2 nanofibers could reach several micrometers. Furthermore, the diameter of NZ1 nanofibers was about 61 ± 11 nm, which was smaller than that of NZ2 nanofibers (68 ± 15 nm). Meanwhile, Figure 2C and D show the energy-dispersive X-ray (EDX) spectra from Figure 2A and B, respectively. It was further confirmed that the NZ1 and NZ2 nanofibers were composed of Ni, Zn, and O. In addition, EDX analysis indicated that the molar ratio of Ni to Zn was about 0.5:1 for NZ1 nanofibers and 1:1 for NZ2 nanofibers, which was close to the theoretical value. The insets of Figure 2C and D were the EDX mappings of Ni, Zn, and O from Figure 2A and B, respectively. It was clearly seen that the Ni, Zn, and O had homogeneous distribution in the NZ1 and NZ2 nanofibers.

In order to study the microstructure of the as-electrospun NiO/ZnO nanofibers, high-resolution transmission electron microscopy (HRTEM) observations were carried out. Figure 3 shows the representative TEM images of the NZ2 nanofibers. The low-magnification TEM image of the NZ2 nanofibers is displayed in Figure 3A. It can be seen that the NZ2 nanofibers are composed of nanoparticles, and each nanoparticle attached to several other nanoparticles. Meanwhile, Figure 3B shows a high-resolution image from the red circle of Figure 3A, which revealed the simultaneous presence of the crystalline NiO and ZnO crystal lattices in the NZ2 nanofibers. The interplanar distances of 0.241 nm were close to the *d* spacings of the (1 1 1) planes of the cubic structured NiO. The interplanar distances of 0.281 nm agreed well with the lattice spacing of the (1 0 0) planes of the hexagonal structured ZnO. Moreover, a distinguished interface and continuity of lattice fringes between the NiO and ZnO nanoparticles can be observed in Figure 3B, suggesting that the *p*−*n* heterojunction might be formed between the NiO and ZnO nanoparticles in the NiO/ZnO nanofibers.

The chemical composition of the as-electrospun NiO, NZ2, and ZnO nanofibers was studied by X-ray photoelectron spectroscopy (XPS) analysis, and the corresponding

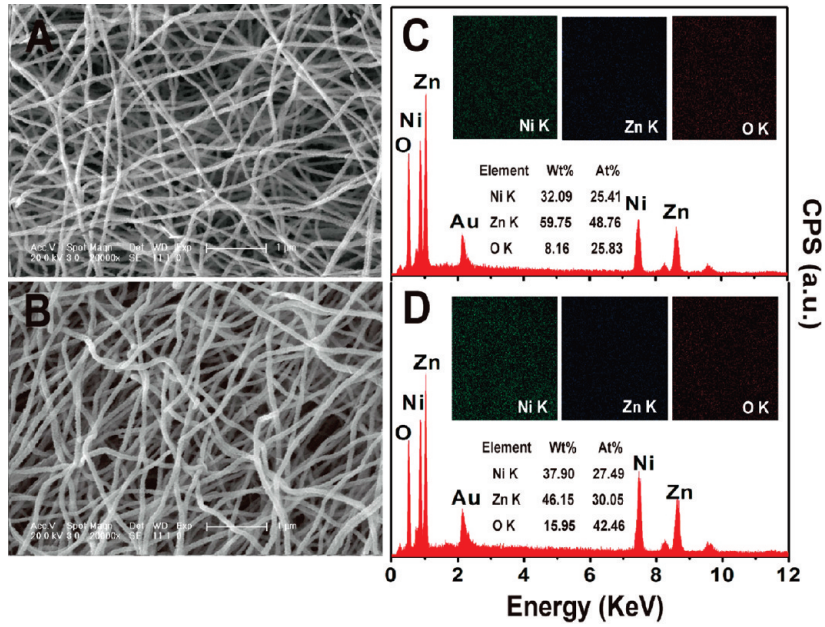

FIGURE 2. SEM image of as-electrospun nanofibers (A), NZ1 nanofibers, and (B) NZ2 nanofibers. (C) EDX spectrum from image A. The insets show the elemental maps of Ni, Zn, and O concentrations in image A. (D) EDX spectrum from image B. The insets were the elemental maps of Ni, Zn, and O concentrations in image B.

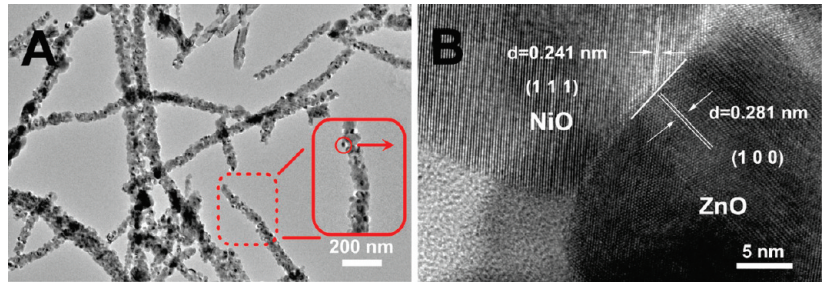

FIGURE 3. (A) TEM image of the as-electrospun NZ2 nanofibers; (B) HRTEM of *p*-type NiO/*n*-type ZnO heterojunction region in the NZ2 nanofibers.

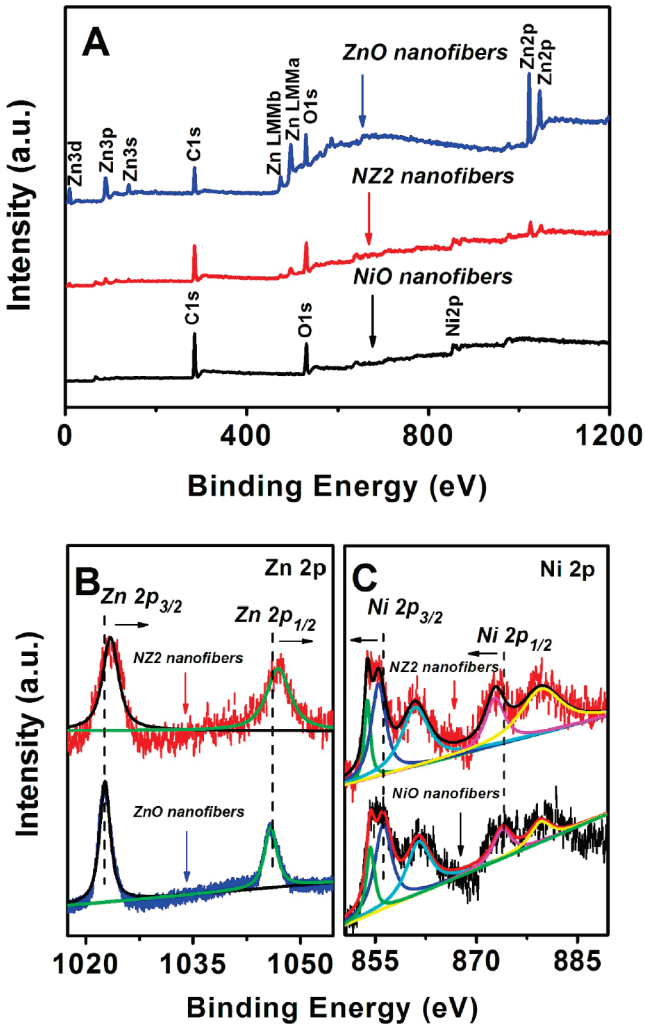

FIGURE 4. XPS spectra of the as-electrospun NiO, NZ2, and ZnO nanofibers: (A) XPS full spectrum, (B) Zn 2p spectra, (C) Ni 2p spectra.

results are shown in Figure 4. As observed in Figure 4A, the fully scanned spectra indicate that Ni, O, and C existed in the NiO nanofibers, while Zn, O, and C existed in ZnO nanofibers. Furthermore, all of the peaks on the curves of the NZ2 nanofibers were ascribed to Ni, Zn, O, and C, and no peaks of other elements were are observed. The C element could be attributed to the adventitious carbon-based contaminant, and the binding energy for the C 1s peak at 284.6 eV was used as the reference for calibration. Therefore, it was concluded that the NZ2 nanofibers were composed of three elements, Ni, Zn, and O, which was in good agreement with the above XRD and EDX results. Subsequently, the Zn 2p high-resolution XPS spectra of the ZnO and NZ2 nanofibers are analyzed in Figure 4B. For ZnO nanofibers, there were two symmetric peaks in the Zn 2p region. The peak centered at 1021.8 eV corresponded to the Zn $2p_{3/2}$, and another one centered at 1044.9 eV was assigned to Zn $2p_{1/2}$ (27). Interestingly, in Figure 4B, the binding energy of Zn 2p ($2p_{3/2}$ and $2p_{1/2}$) for the NZ2 nanofibers shifts remarkably to the higher binding energy (about 0.9 eV) compared with the corresponding value for ZnO nanofibers. However, the observed spin-orbit splitting of Zn 2p (between Zn $2p_{3/2}$ and Zn $2p_{1/2}$) for the NZ2 nanofibers is about 23 eV, which is consistent with the corresponding value of pure ZnO nanofibers, indicating a normal state of Zn^{2+} in the ZnO and NZ2 nanofibers (28, 29). Figure 4C shows the Ni 2p high-resolution XPS spectra of the NiO and NZ2 nanofibers. As observed in Figure 4C, the Ni 2p signal of NiO nanofibers could be deconvoluted into five peaks. The binding energies at 854.2, 856.1, and 861.4 eV were attributed to the Ni $2p_{3/2}$ peaks, and the 873.8 and 879.5 eV peaks were attributed to the Ni $2p_{1/2}$ peaks. The Ni $2p_{3/2}$ peaks were assigned to Ni^{2+} ions in the NiO nanofibers (30). The peak at 854.2 eV was due to NiO_6 in octahedral symmetry, and the peak at 856.1 eV was attributed to NiO_5 or Ni^{2+} in pyramidal symmetry according to the experimental results and theoretical calculation of Sorian et al. (31). In Figure 4C, similar to the NiO nanofibers, the Ni 2p signal of the NZ2 nanofibers could also be deconvoluted into five peaks. However, compared with the Ni 2p peaks ($2p_{3/2}$ and $2p_{1/2}$) of NiO nanofibers, the Ni 2p peaks for NZ2 nanofibers shifted toward the lower binding energy with the value about 0.5 eV. Traditionally, the binding energy shifts in the XPS spectra could be explained by two kinds of mechanisms: the different electronegativities of metal ions and the strong interaction (electron transfer) between nanocrystals (11, 23, 32, 33). In our experiment, the electronegativity of the Ni^{2+} ion was about 1.91, which was about 0.26 larger than that of the Zn^{2+} ion. The Ni^{2+} ion could withdraw the electrons from the Zn^{2+} ion, so the screening effect of electrons would decrease for the Zn^{2+} ion but increase for the Ni^{2+} ion. Thus, the Zn 2p peaks shifted toward the higher binding energy, while the Ni 2p peaks shifted to the lower binding energy. It was suggested that there might be Ni−O−Zn bonds present at the interface between the NiO and ZnO nanoparticles, which further confirmed the TEM results. In addition, when the NiO and ZnO nanoparticles

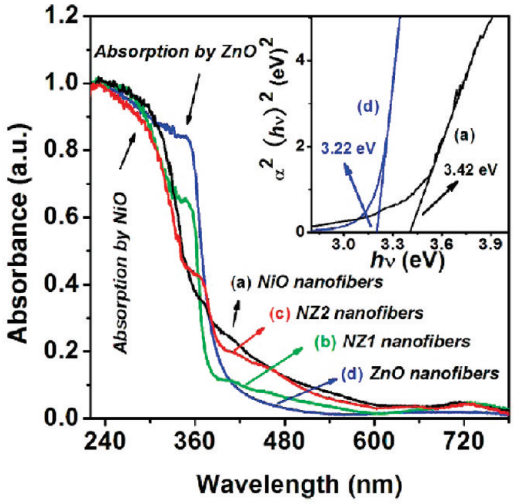

FIGURE 5. UV−vis diffuse reflectance (DR) spectra of the as-electrospun nanofibers: (a) NiO nanofibers, (b) NZ1 nanofibers, (C) NZ2 nanofibers, (d) ZnO nanofibers. The inset shows the plots of the $(\alpha h\nu)^2$ vs photon energy ($h\nu$) for ZnO and NiO nanofibers.

attach together, electron transfer could occur from the *n*-type ZnO to *p*-type NiO nanoparticle until the system attains equilibration. Therefore, the Zn 2p and Ni 2p peaks in our experiment shifted toward the higher and lower binding energies, respectively. It was indicated that there might exist a strong interaction between the *p*-type NiO and *n*-type ZnO nanoparticles. These results indicated the formation of *p*−*n* heterojunctions in the NiO/ZnO nanofibers.

Figure 5 shows the UV−vis diffuse reflectance (DR) spectroscopy of the NiO, NZ1, NZ2, and ZnO nanofibers. As shown in Figure 5a and d, the strong absorption peaks of the as-electrospun NiO and ZnO nanofibers were located at about 305 and 355 nm, respectively (27, 34). Furthermore, a weak absorption peak with a maximum around 720 nm was observed in NiO nanofibers, which could be assigned to intra-3d transitions of Ni^{2+} in the cubic crystal field of NiO (35−37). In Figure 5b and c, all of the characteristic absorption peaks of NiO and ZnO existed in the UV−vis DR spectroscopy of the NZ1 and NZ2 nanofibers. It was confirmed that the NiO/ZnO nanofibers were composite materials that consisted of NiO and ZnO. The band gap energy of the NiO and ZnO nanofibers was calculated by eq 1 (38):

$$\alpha h\nu = A(h\nu - E_g)^{n/2} \quad (1)$$

where α, ν, E_g, and A are the absorption coefficient, light frequency, band gap, and a constant, respectively. Moreover, n depends on the characteristics of the transition in a semiconductor: direct transition ($n = 1$) or indirect transition ($n = 4$). For NiO and ZnO, the value of n was 1 for the direct transition (18). Therefore, the band gap energy of the NiO and ZnO nanofibers in our experiment could be estimated from a plot of $(\alpha h\nu)^2$ versus photon energy $h\nu$. As observed in the inset of Figure 5, the band gap of NiO was evaluated to be 3.42 eV, while the band gap of ZnO was found to be about 3.22 eV. Those values were close to the reported values of NiO (3.5 eV) and ZnO (3.37 eV) (8, 18).

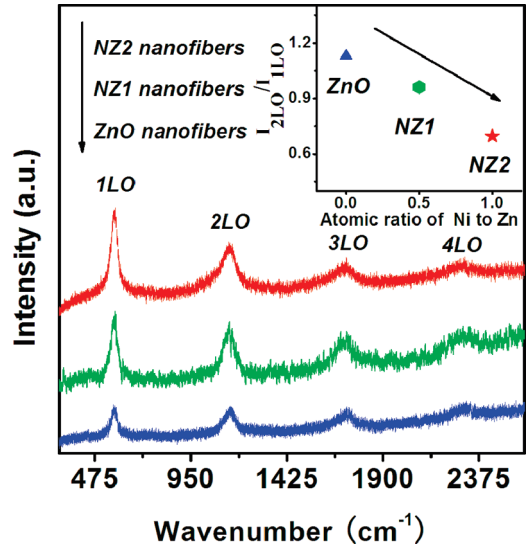

FIGURE 6. Resonant Raman scattering spectra of ZnO, NZ1, and NZ2 nanofibers. The inset shows the intensity ratio between the second- and the first-order Raman scattering as a function of the atomic ratio of Ni/Zn in the above nanofibers.

Figure 6 shows the resonant Raman scattering spectroscopy of the ZnO, NZ1, and NZ2 nanofibers. It could be seen that the main peaks of the 1−4 longitudinal optical (LO) phonon mode for ZnO nanoparticles appeared in all three electrospun nanofibers. It is known that the electron−phonon interaction could be probed by resonant Raman scattering when the exciting photon energy was resonant with the electronic interband transition energy of the wurtzite ZnO. In the experiment, the above electrospun nanofibers were excited by the 325 nm line (3.81 eV) of a He−Cd laser. According to the results of the UV−vis DR spectra, the band gap of ZnO nanoparticles was about 3.22 eV in our present work. It meant that the multiphonon scattering was easily observed in the resonant Raman spectra of the ZnO, NZ1, and NZ2 nanofibers. According to the theory of polar optical phonons in wurtzite nanocrystals, the LO phonon mode in disordered oriented ZnO nanoparticles should be a mixture of A_1-LO (574 cm^{-1}) and E_1-LO (583 cm^{-1}) (39). In Figure 6, four major bands of LO phonon modes centered around 577, 1140, 1723, and 2297 cm^{-1} are observed to result mainly from the polar symmetry modes A_1-LO and E_1-LO and their overtones. Furthermore, in the inset of Figure 6, the integrated intensity ratios (after subtracting the background) between the second- and the first-order LO Raman scatterings (I_{2LO}/I_{1LO}) are found to decrease remarkably from 1.13 to 0.69, while an increase of the Ni/Zn molar ratios in the electrospun nanofibers occurs from 0 to 1. The LO Raman scattering included contributions from both the deformation potential and Fröhlich potential that involved the long-range interaction generated by the macroscopic electric field associated with the LO phonons (40−42). It had been reported that the coupling strength between the electron and LO phonon (deduced from the ratio of the second- to the first-order Raman scattering intensity) weakened with a decrease in the grain size of ZnO nanocrystals (42). However, the grain size of ZnO nanoparticles in ZnO, NZ1, and NZ2 electrospun nanofibers was about 32.4, 31.4, and 29.6 nm

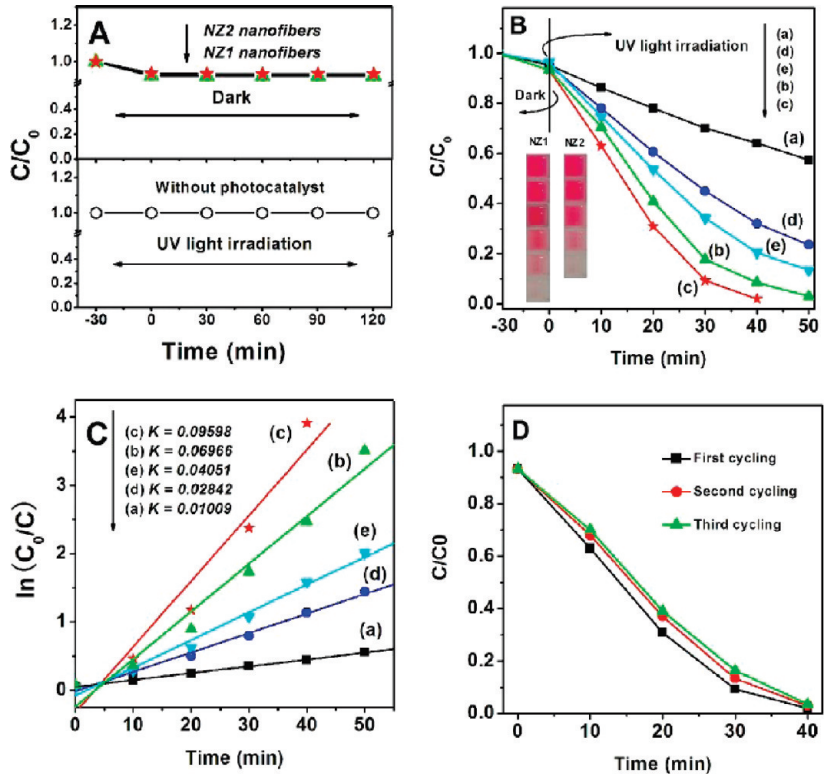

FIGURE 7. (A) Degradation profiles of RB in the presence of the NZ1 and NZ2 nanofiber photocatalysts but in the dark and with UV light irradiation but in the absence of the nanofiber photocatalysts. (B) Degradation profiles of RB over different nanofibers. The inset illustrates the comparison of the RB solutions photodegraded with NZ1 and NZ2 nanofibers (C_0 = 10 mg/L, catalyst 0.01 g). (C) Kinetic linear simulation curves of RB photocatalytic degradation with different electrospun nanofibers: (a) NiO nanofibers, (b) NZ1 nanofibers, (c) NZ2 nanofibers, (d) ZnO nanofibers, (e) TiO_2 nanofibers. (D) Photocatalytic activity of the NZ2 nanofibers for RB degradation with three time cycling uses.

from the results of XRD. It was suggested that the decreasing of I_{2LO}/I_{1LO} could hardly be ascribed to the grain size of the ZnO nanoparticles in our experiment but might come from the inner electric field in the interface of *p*-type NiO and *n*-type ZnO nanoparticles due to the electron transfer between NiO and ZnO nanoparticles.

To demonstrate the photoactivity of the as-electrospun nanofibers of *p*-type NiO/*n*-type ZnO heterojunctions for the degradation of organic pollutants, we carried out experiments of the photocatalytic degradation of rhodamine B (RB) as a test reaction. As observed in Figure 7A, the control experiments were performed on the *p*-type NiO/*n*-type ZnO heterojunction nanofibers (NZ1 and NZ2 nanofibers) under different conditions: (1) in the presence of nanofiber photocatalysts but in the dark and (2) with UV light irradiation but in the absence of the nanofiber photocatalysts. These results revealed that there was no appreciable degradation of RB after 120 min either in the absence of UV light irradiation or in the absence of nanofiber photocatalysts. However, in Figure 7B, an obvious degradation of RB was observed under UV light in the presence of the NZ1 and NZ2 nanofibers. Furthermore, in the comparative experiments, the NiO, ZnO, and TiO_2 electrospun nanofibers were used as a photocatalytic reference to understand the photocatalytic activity of the *p*-type NiO/*n*-type ZnO heterojunction nanofibers. As shown in Figure 7B, the degradation efficiency of RB was about 42.6, 99.7, 76.4, and 86.6% for the NiO, NZ1, ZnO, and TiO_2 nanofibers after 50 min, respectively. Notably, the time for an entire decolorization of RB over the NZ2 nanofibers was only about 40 min, which was much shorter than the corresponding degradation time of NiO, NZ1, ZnO, and TiO_2 nanofibers, suggesting that the NZ2 nanofibers exhibited the highest photocatalytic activity among those nanofiber nanocatalysts. For a better comparison of the photocatalytic efficiency of the above electrospun nanofibers, the kinetic analysis of degradation of RB was discussed. The kinetic linear simulation curves of the photocatalytic degradation of RB over the above nanofiber photocatalysts showed that the above degradation reactions followed a Langmuir−Hinshelwood apparent first-order kinetics model due to the low initial concentrations of the reactants. The explanation is described below (43):

$$r = dC/dt = kKC/(1 + KC) \quad (2)$$

where r is the degradation rate of the reactant (mg/(L min)), C is the concentration of the reactant (mg/L), t is the UV light irradiation time, k is the reaction rate constant (mg/(L min)), and K is the adsorption coefficient of the reactant (L/mg). When the initial concentration (C_0) is very low (C_0 = 10 mg/L for RB in the present experiment), eq 2 can be simplified to an apparent first-order model (44):

$$\ln C_0/C = kKt = k_{app}t \quad (3)$$

where k_{app} is the apparent first-order rate constant (min^{-1}). The determined k_{app} for different catalysts is summarized

Scheme 1. Schematic Diagram Showing the Energy Band Structure and Electron−Hole Pair Separation in the *p*-Type NiO/*n*-Type ZnO Heterojunction

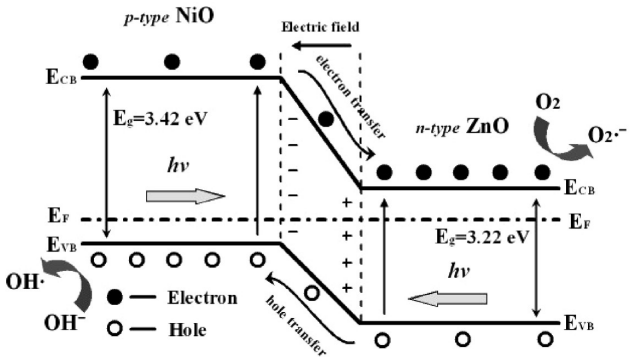

in Figure 7C. It was indicated that the photocatalytic reactivity order was NZ2 nanofibers > NZ1 nanofibers > TiO_2 nanofibers > ZnO nanofibers > NiO nanofibers, which was consistent with the activity studies above. Moreover, Figure 7D showed the photocatalytic degradation of RB over the NZ2 nanofibers under UV light irradiation with three time cycling uses. It was indicated that those nanofiber photocatalysts with high photocatalytic activity could be easily recovered by sedimentation and would greatly promote their industrial application in eliminating organic pollutants from wastewater.

On the basis of the above experimental results and the theory analysis, a proposed energy band structure diagram of the *p*-type NiO/*n*-type ZnO heterojunction is elucidated schematically in Scheme 1. When the *p*-type NiO and *n*-type ZnO formed the *p*−*n* heterojunction, the electron transfer occurred from ZnO to NiO while the hole transfer occurred from NiO to ZnO until the system attained equilibration due to the carrier diffusion between the NiO and ZnO. Meanwhile, an inner electric field was built in the interface between NiO and ZnO because of the electron and hole transfers. When the *p*-type NiO and *n*-type ZnO heterojunction was excited by UV light with a photon energy higher or equal to the band gaps of NiO and ZnO, the electrons in the VB could be excited to the CB with simultaneous generation of the same amount of holes in the VB. From the energy band structure diagram of the *p*-type NiO and *n*-type ZnO heterojunction in Scheme 1, it can be found that the photogenerated electron transfer occurred from the CB of NiO to the CB of ZnO and, conversely, the photogenerated hole transfer could take place from the VB of ZnO to the VB of NiO, suggesting that the photogenerated electrons and holes were efficiently separated. Furthermore, the better separation of photogenerated electrons and holes in the *p*-type NiO and *n*-type ZnO heterojunction was confirmed by comparing the PL and SPS spectra of the ZnO and NZ1 and NZ2 nanofibers. In Figure 8A, it is shown that the NZ1 and NZ2 nanofibers exhibited much lower emission intensity than ZnO nanofibers, indicating that the recombination of the photogenerated charge carrier was inhibited greatly in the *p*-type NiO and *n*-type ZnO heterojunction. Further investigation found that the NZ2 nanofibers appeared lower in emission intensity than NZ1 nanofibers, suggesting a high separation efficiency of photogerenated electron−hole pairs. Meanwhile, as observed in the inset of Figure 8A, the normalized PL spectra for ZnO, NZ1, and NZ2 nanofibers indicated that the visible emission of NZ1 and NZ2 nanofibers was obvious higher than that of ZnO nanofibers, which might be attributed to the increase of the surface oxygen vacancy defects of ZnO nanoparticles in the *p*-type NiO/*n*-type ZnO heterojunction nanofibers. According to the literature (45), the oxygen vacancy defects on the surface of ZnO nanocrystals benefited the separation efficiency of photogenerated electron−hole pairs. To further confirm the efficient charge separation in *p*-type NiO and *n*-type ZnO heterojunction nanofibers, we carried out an SPS experiment, and the results are shown in Figure 8B. All samples had a clearly SPS response, indicating that the photon absorption indeed induced the charge generation and separation. By comparing the SPS peak of ZnO nanofibers, the *p*-type NiO/*n*-type ZnO heterojunction nanofibers showed the bule-shift with an increase in the molar ratios of Ni to Zn. Furthermore, the SPS response range increased with an increase in the Ni/Zn molar ratios in the *p*-type NiO/*n*-type ZnO heterojunction nanofibers. It was implied that the separation efficiency of photogenerated electron−hole pairs was improved. The efficient charge separation could increase the lifetime of the charge carriers and enhance the efficiency of the interfacial charge transfer to adsorbed substrates and then account for the higher activity of the *p*-type NiO and *n*-type ZnO heterojunction nanofibers. The

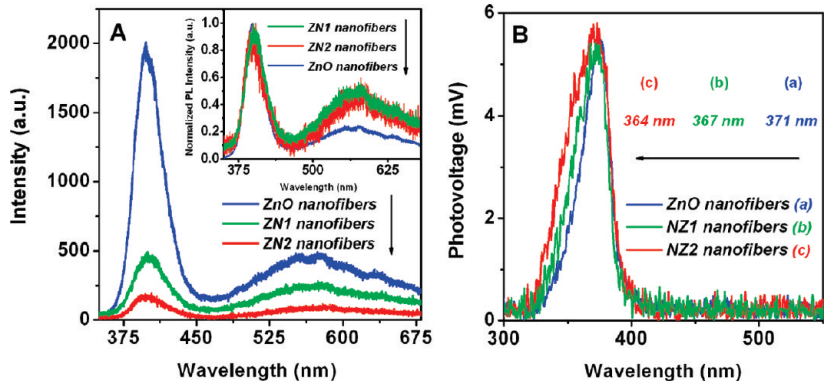

FIGURE 8. (A) PL emission spectra of ZnO, NZ1, and NZ2 nanofibers. The inset shows the normalized PL spectra of ZnO, NZ1, and NZ2 nanofibers. (B) Surface photovoltage spectroscopy of ZnO, NZ1, and NZ2 nanofibers.

photocatalytic mechanism in our experiment is proposed as follows:

$$(p\text{-type NiO}/n\text{-type ZnO}) + h\nu \xrightarrow{\text{UV}} e^-(\text{ZnO}) + h^+(\text{NiO})$$

$$e^- + O_2 \rightarrow O_2^{\bullet -}$$

$$h^+ + OH^- \rightarrow OH^\bullet$$

$$O_2^{\bullet -} + H_2O \rightarrow HO_2^\bullet + OH^-$$

$$HO_2^\bullet + H_2O \rightarrow H_2O_2 + OH^\bullet$$

$$H_2O_2 \rightarrow 2OH^\bullet$$

$$OH^\bullet + RB \rightarrow CO_2 + H_2O$$

Under UV light irradiation, the photogenerated electrons moved to the ZnO side; meanwhile, the photogenerated holes moved to the NiO side. Afterward, the holes were ultimately trapped by surface hydroxyl groups (or H_2O) at the catalyst surface to yield $OH^\bullet$ radicals. The dissolved oxygen molecules reacted with the electrons to yield superoxide radical anions, $O_2^{\bullet -}$, which on protonation generated the hydroperoxy, $HO_2^\bullet$, radicals, producing hydroxyl radical $OH^\bullet$, which was a strong oxidizing agent for decomposing the organic dye (46, 47).

CONCLUSION

In summary, by using a sol−gel process and electrospinning technology, *p*-type NiO/*n*-type ZnO heterojunction nanofibers with different molar ratios of Ni to Zn were successfully fabricated. The investigation of photocatalytic ability indicated that the *p*-type NiO/*n*-type ZnO heterojunction nanofibers possessed higher photocatalytic activity than the pure NiO and ZnO nanofibers for the degradation of RB dye under UV light irradiation due to the enhanced separation efficiency of photogenerated electron−hole pairs from the *p*−*n* heterojunctions. In addition, these nanofibers could be easily recycled without a decrease in the photocatalytic activity due to their one-dimensional nanostructure properties. Also, it is expected that the *p*-type NiO/*n*-type ZnO heterojunction nanofibers with high photocatalytic activity will greatly promote their industrial application in the elimination of organic pollutants from wastewater.

Acknowledgment. The present work is supported financially by the National Natural Science Foundation of China (Nos. 50572014, 50972027, and 10647108) and the Program for New Century Excellent Talents in University (NCET-05-0322).

REFERENCES AND NOTES

(1) Yoneyama, H.; Yamashita, Y.; Tamura, H. *Nature* **1979**, *282*, 817.
(2) Asahi, R.; Morikawa, T.; Ohwaki, T.; Aoki, K.; Taga, Y. *Science* **2001**, *293*, 269.
(3) Hoffmann, M. R.; Martin, S. T.; Choi, W.; Bahnemannt, D. W. *Chem. ReV.* **1995**, *95*, 69.
(4) Testino, A.; Bellobono, I. R.; Buscaglia, V.; Canevali, C.; D'Arienzo, M.; Polizzi, S.; Scotti, R.; Morazzoni, F. *J. Am. Chem. Soc.* **2007**, *129*, 3564.
(5) Katsumata, K.; Cordonier, C. E. J.; Shichi, T.; Fujishima, A. *J. Am. Chem. Soc.* **2009**, *131*, 3856.
(6) Jang, E. S.; Won, J. H.; Hwang, S. J.; Choy, J. H. *Adv. Mater.* **2006**, *18*, 3309.
(7) Mclaren, A.; Valdes-Solis, T.; Li, G.; Tsang, S. C. *J. Am. Chem. Soc.* **2009**, *131*, 12540.
(8) Wang, Z. L. *ACS Nano* **2008**, *2*, 1987.
(9) Xu, L.; Hu, Y.; Pelligra, C.; Chen, C.; Jin, L.; Huang, H.; Sithambaram, S.; Aindow, M.; Joesten, R.; Suib, S. L. *Chem. Mater.* **2009**, *21*, 2875.
(10) Zheng, L.; Zheng, Y.; Chen, C.; Zhan, Y.; Lin, X.; Zheng, Q.; Wei, K.; Zhu, J. *Inorg. Chem.* **2009**, *48*, 1819.
(11) Zheng, Y.; Zheng, L.; Zhan, Y.; Lin, X.; Zheng, Q.; Wei, K. *Inorg. Chem.* **2007**, *46*, 6980.
(12) Wang, Q.; Geng, B.; Wang, S. *Environ. Sci. Technol.* **2009**, *43*, 8968.
(13) Lei, Y.; Zhao, G.; Liu, M.; Zhang, Z.; Tong, X.; Cao, T. *J. Phys. Chem. C* **2009**, *113*, 19067.
(14) Wang, X.; Liu, G.; Chen, Z.; Li, F.; Wang, L.; Lu, G. Q.; Cheng, H. *Chem. Commun.* **2009**, 3452.
(15) Hameed, A.; Montini, T.; Gombac, V.; Fornasiero, P. *Photochem. Photobiol. Sci.* **2009**, *8*, 677.
(16) Ohta, H.; Hirano, M.; Nakahara, K.; Maruta, H.; Tanabe, T.; Kamiya, M.; Kamiya, T.; Hosono, H. *Appl. Phys. Lett.* **2003**, *83*, 1029.
(17) Wang, J.; Lee, C.; Chen, Y.; Chen, C.; Chen, Y.; Lin, C.; Chen, Y. *Appl. Phys. Lett.* **2009**, *95*, 131117.
(18) Gupta, R. K.; Ghosh, K.; Kahol, P. K. *Physica E* **2009**, *41*, 617.
(19) Chen, S.; Zhang, S.; Liu, W.; Zhao, W. *J. Hazard. Mater.* **2008**, *155*, 320.
(20) Wang, C.; Shao, C.; Wang, L.; Zhang, L.; Li, X.; Liu, Y. *J. Colloid Interface Sci.* **2009**, *333*, 242.
(21) Wang, C.; Shao, C.; Liu, Y.; Zhang, L. *Scr. Mater.* **2008**, *59*, 332.
(22) Liu, Z.; Sun, D. D.; Guo, P.; Leckie, J. O. *Nano Lett.* **2007**, *7*, 1081.
(23) Lin, D.; Wu, H.; Zhang, R.; Pan, W. *Chem. Mater.* **2009**, *21*, 3479.
(24) Zhang, Z.; Shao, C.; Li, X.; Zhang, L.; Xue, H.; Wang, C.; Liu, Y. *J. Phys. Chem. C* **2010**, *114*, 7920.
(25) Liu, Z.; Sun, D. D.; Guo, P.; Leckie, J. O. *Nano Lett.* **2007**, *7*, 1081.
(26) Lin, Y.; Wang, D.; Zhao, Q.; Yang, M.; Zhang, Q. *J. Phys. Chem. B* **2004**, *108*, 3202.
(27) Liu, Y.; Zhong, M.; Shan, G.; Li, Y.; Huang, B.; Yang, G. *J. Phys. Chem. B* **2008**, *112*, 6484.
(28) Ghosh, K.; Kumar, M.; Wang, H.; Maruyama, T.; Ando, Y. *Langmuir* **2010**, *26*, 5527.
(29) Moulder, J. F.; Stickle, W. F.; Sobol, P. E.; Bomben, K. D. *In Handbook of X-ray Photoelectron Spectroscopy*; Chastain, J., Ed.; Perkin-Elmer Corp.: New York, 1992.
(30) Zhao, B.; Ke, X.; Bao, J.; Wang, C.; Dong, L.; Chen, Y.; Chen, H. *J. Phys. Chem. C* **2009**, *113*, 14440.
(31) Soriano, L.; Preda, I.; Gutieŕrez, A.; Palac1ń, S. *Phys. ReV. B: Condens. Matter Mater. Phys.* **2007**, *75*, 233417.
(32) Bae, S. Y.; Choi, H. C.; Na, C. W.; Parka, J. *Appl. Phys. Lett.* **2005**, *86*, 033102.
(33) Chen, W.; Qiu, Y.; Zhong, Y.; Wong, K. S.; Yang, S. *J. Phys. Chem. A* **2010**, *114*, 3127.
(34) Subramanian, B.; MohamedIbrahim, M.; Senthilkumar, V.; Murali, K. R.; Vidhya, VS.; Sanjeeviraja, C.; Jayachandran, M. *Physica B* **2008**, *403*, 4104.

(35) Adler, D.; Feinlieb, J. *Phys. ReV. B* **1970**, *2*, 3112.
(36) Tsuboi, T.; Kleeman, W. *J. Phys.: Condens. Matter* **1994**, *6*, 8625.
(37) Boschloo, G.; Hagfeldt, A. *J. Phys. Chem. B* **2001**, *105*, 3039.
(38) Butler, M. A. *J. Appl. Phys.* **1977**, *48*, 1914.
(39) Zhang, X. H.; Liu, Y. C.; Wang, X. H.; Chen, S. J.; Wang, G. R.; Zhang, J. Y.; Lu, Y. M.; Shen, D. Z.; Fan, X. W. *J. Phys.: Condens. Matter* **2005**, *17*, 3035.
(40) Loudon, R. *Adv. Phys.* **1964**, *13*, 23.
(41) Kaminow, I. P.; Johnston, W. D. *Phys. Rev.* **1967**, *160*, 19.
(42) Cheng, H.; Lin, K.; Hsu, H.; Hsieh, W. *Appl. Phys. Lett.* **2006**, *88*, 261909.
(43) Turchi, C. S.; Ollis, D. F. *J. Catal.* **1990**, *122*, 178.
(44) Lee, M. S.; Park, S. S.; Lee, G.-D.; Ju, C.-S.; Hong, S.-S. *Catal.Today* **2005**, *101*, 283.
(45) Zheng, Y.; Chen, C.; Zhan, Y.; Lin, X.; Zheng, Q.; Wei, K.; Zhu, J. *J. Phys. Chem. C* **2008**, *112*, 10773.
(46) Aarthi, T.; Madras, G. *Ind. Eng. Chem. Res.* **2007**, *46*, 7.
(47) Rajeshwar, K.; Osugi, M. E.; Chanmanee, W.; Chenthamarakshan, C. R.; Zanoni, M. V. B.; Kajitvichyanukul, P.; Krishnan-Ayer, R. *J. Photochem. Photobiol., C* **2008**, *9*, 171.

AM100618H